ELSEVIER

Soil Dynamics and Earthquake Engineering 25 (2005) 513–527

SOIL DYNAMICS AND EARTHQUAKE ENGINEERING

www.elsevier.com/locate/soildyn

# Wave propagation and soil–structure interaction on a cliff crest during the 1999 Athens Earthquake

Dominic Assimaki[a,*], Eduardo Kausel[b,1], George Gazetas[c,2]

[a]*Institute for Crustal Studies, University of California, Santa Barbara, CA, USA*
[b]*Department of Civil and Environmental Engineering, Massachusetts Institute of Technology, Rm. 1-271, 33, Massachusetts Avenue, Cambridge, MA 02139, USA*
[c]*School of Civil Engineering, National Technical University of Athens, Greece*

Received 15 April 2004; revised 1 October 2004; accepted 1 November 2004

**Abstract**

During the 1999 Athens Earthquake the town of Adàmes, located on the eastern cliff of the Kifissos river canyon, experienced unexpectedly heavy damage. Despite the significant amplification potential of the slope geometry, topography effects cannot alone explain the uneven damage distribution within a 300 m zone behind the crest, characterized by a rather uniform structural quality. This paper illustrates the important role of soil stratigraphy, material heterogeneity, and soil–structure interaction on the characteristics of ground surface motion. For this purpose, we first perform elastic two-dimensional wave propagation analyses utilizing available geotechnical and seismological data, and validate our results by comparison with aftershock recordings. We then conduct non-linear time-domain simulations that include spatial variability of soil properties and soil–structure interaction effects, to reveal their *additive* contribution in the topographic motion aggravation.


*Keywords:* Topography; Stratigraphy; 2D wave propagation; Inelastic soil behavior; Random properties; Soil–structure interaction; Cliff crest; Case study

## 1. Introduction

It has been recognized that topography can significantly affect the amplitude and frequency characteristics of ground motion, as well as its spatial variability, during seismic events. In the recent past, documented observations from destructive seismic events show that buildings located at the tops of hills, ridges and canyons, suffer more intensive damage than those located at the base: the Lambesc Earthquake [France, 1909], the San Fernando Earthquake [1971], the Friuli Earthquake, [Italy, 1976], the Irpinia Earthquake [Italy, 1980], the Chile Earthquake [1985], the Whittier Narrows Earthquake [1987], the 'Eje-Cafetero' Earthquake [Colombia, 1998] and recent earthquakes in Greece [Kozani, 1995 and Athens, 1999] and Turkey [Bingöl, 2003] are only some examples of catastrophic events, during which severe structural damage has been reported on hilltops or close to steep slopes.

Topographic amplification is still understood imperfectly, and the insufficient number of documented evidence prevents these effects from being incorporated in most seismic code provisions and microzonation studies. Instrumental studies that have been performed in recent years verify the macroseismic observations, by predicting systematic amplification of seismic motion over convex topographies such as hills and ridges, deamplification over concave topographic features such as canyons and hill toes, and complex amplification and deamplification patterns on hill slopes. The problem of scattering and diffraction of seismic waves by topographical irregularities has been also studied by many authors. The majority of these studies focus on two-dimensional simulations in which the topographic asperities are treated as isolated ridges or depressions,

* Corresponding author. Address: Department of Civil and Environmental Engineering, Georgia Institute of Technology, 790, Atlantic Drive, Atlanta, GA 30332, USA. Tel.: +1 617 510 7579.

*E-mail addresses:* dominic@crustal.ucsb.edu (D. Assimaki), kausel@mit.edu (E. Kausel), gazetas@ath.forthnet.gr (G. Gazetas).

[1] Tel.: +1 617 253 5336.

[2] Present address: 2, Giavassi Street, Agia Paraskeui, 15342 Athens, Greece. Tel.: +30 210 6008578.

0267-7261/$ - see front matter © 2005 Elsevier Ltd. All rights reserved.
doi:10.1016/j.soildyn.2004.11.031

usually on the surface of homogeneous elastic media. Comparison between instrumental and theoretical results reveals that there is indeed *qualitative* agreement between theory and observations on topography effects. Nevertheless, from a *quantitative* viewpoint, there still exists clear discrepancy in numerous cases, where the observed amplification of weak motion is significantly larger than the theoretical predictions. Apparently, results from instrumental studies on weak motion data or ambient noise may not be applicable to describe topography effects for strong ground shaking, which is usually associated with inelastic soil response. Indeed, there exist very few—if any—well documented case studies where topography effects are illustrated for strong ground motion.

This paper uses a case-study from the Athens 1999 earthquake to illustrate the decisive role of local stratigraphy, material heterogeneity and soil–structure interaction in altering the energy focusing mechanism at the vertex of convex topographies. The effects of local soil conditions are validated by comparison with weak motion data. The effects of inelastic soil behavior and non-linear soil–structure interaction are then illustrated for the strong-motion recordings. Our conclusions can be used as guideline for more rigorous analyses to be performed, accounting for the *additive* contribution of engineering issues in the extensively studied seismological problem of topographic motion amplification. This study is a continuation of the studies in Refs. [2–5].

## 2. The 7-Sept-99 earthquake

The $M_s$ 5.9 event that shook Athens just 3 weeks after the $M_s$ 7.4 Kocaeli Earthquake has been characterized as the worst natural disaster in the modern history of Greece. This moderate event had a major socio-economical impact, resulting in the loss of 150 lives, the collapse of 100 residential and industrial buildings and the severe damage of another 6000. In the two-and-a-half millennia of history no earthquake has ever been assigned to or near the 1999 seismogenic fault. The location of the ruptured fault and the geography of the heavily damaged region, are schematically illustrated in Fig. 1. Also shown in the same figure are the locations of the four accelerograph stations, which recorded the strongest motions: KEDE, MNSA, SGMA, and SPLB (Refs. [2,4]).

### 2.1. Adàmes: observations, topography, stratigraphy

One of the most heavily damaged areas was the small community of Adàmes, located next to the deepest canyon of Kifissos river, the main river of the Athens metropolitan area. The majority of local buildings, constructed in the 1970s and early 1980s, comprise 2- to 4-storey concrete reinforced structures of rather uniform quality. Nevertheless, the MMI in the 1200 m long and 300 m wide town

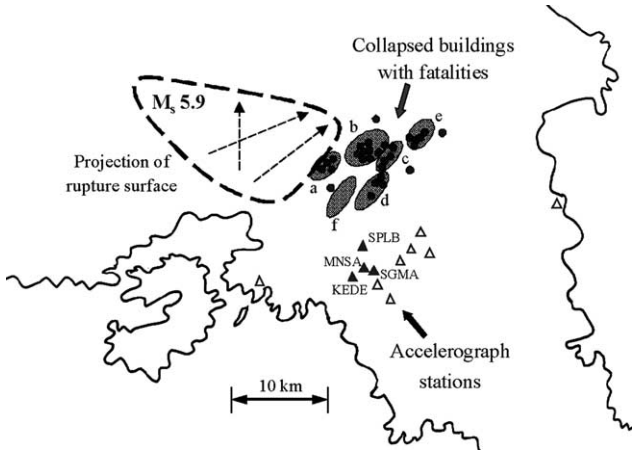


Fig. 1. Sketch of the map of the earthquake stricken region showing the surface projection of the fault. The triangles indicate the location of accelerograph stations, four of which (shown with filled triangles) are utilized in our study. The circles show the location of the 28 collapsed buildings with human casualties (Ref. [2]).

ranged from $VII^+$ to $VIII^+$, despite its 8–10 km distance from the projection of the causative fault [2].

The location of the town next to the crest of the canyon in conjunction with the high damage intensity (as opposed to numerous other towns located at equal or smaller distances from the source where MMI did not exceed a mere VII) brought forward topography effects to justify the macroseismic observations. Behind the crest, however, damage was non-uniform: in the parallel to the river axis direction, it was concentrated in two zones, one next to the crest and one at a distance about 200–300 m from it. Some scattered—yet less intense—damage was observed at intermediate locations. It seems therefore, that focusing of seismic energy at the vertex certainly played a significant role, but was not the only phenomenon involved.

A topographic survey of the canyon produced the cross-section shown in Fig. 2. The slightly idealized geometry of the canyon used in our investigation is also shown in this figure. Note the 40 m deep and the nearly 2:1 (horizontal to vertical) slope of the canyon cliff.

Geotechnical investigations of the area comprised the drilling of 10 boreholes with Standard Penetration Blow Count ($N_{SPT}$) measurements and laboratory testing for the definition of the variation of plasticity index ($I_p$) with depth. Eight of these were performed down to a depth of about 35 m, and two reached almost 80 m. Some indirect evidence for greater depths was 'extrapolated' from two 150-m-deep boreholes drilled for the under-construction Olympic Village, 1.5 km west to northwest of Adàmes. The overall picture emerging from this investigation is shown in Fig. 3, where low-strain shear wave velocity profiles are constructed for three characteristic locations in Adàmes, referred to in the ensuing as profiles A, B, and C. All profiles comprise alternating soil layers of silty-gravely

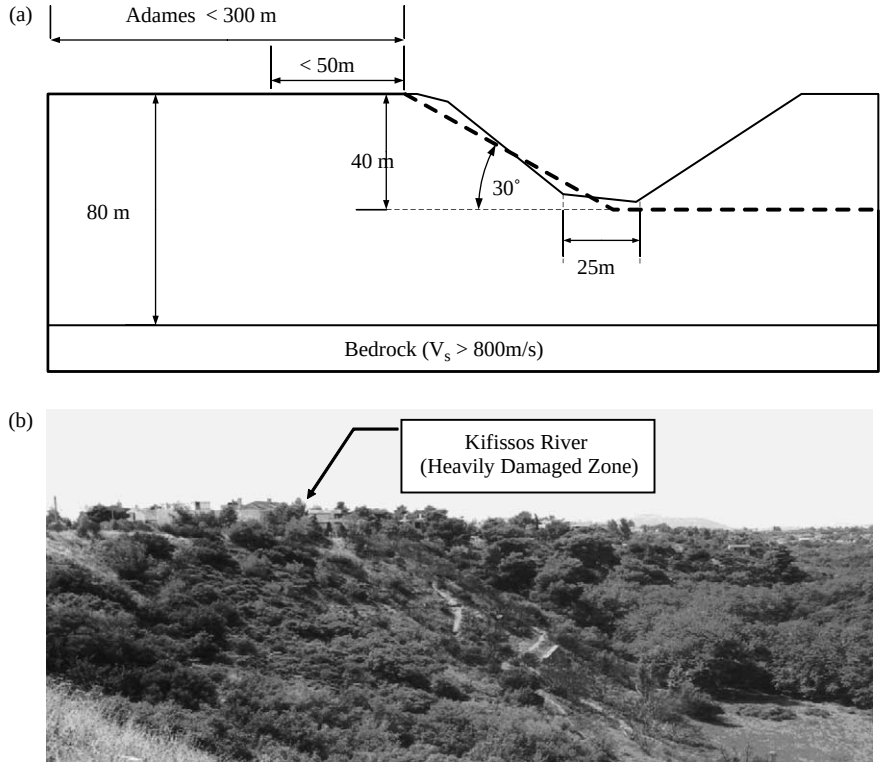


Fig. 2. (a) Typical cross section of the topographic relief of Kifissos river canyon and the region of Adàmes. Site 3 is located 10–50 m behind crest and Site 2 approximately 300 m. The idealized geometry used in our 2D simulations is also shown (dashed line). (b) Bird's eye view of the cliff of the Kifissos canyon (Refs. [2,3]).

sands and sandy-gravely clays in the top 20–30 m. The approximate average velocity, $V_{s,30}$ of the 30 m surface soil layers for the three profiles are: 500 m/s for profile A, 400 m/s for profile B and 340 m/s for profile C, indicative of very stiff (profile A), just stiff (profile B), and moderately stiff (profile C) soil formations according to the European Seismic Code (EC8).

### 2.2. Strong-motion records

Fifteen strong-motion accelerograph stations were triggered by the main shock within 25 km from the causative fault, recording peak ground accelerations (PGA) that ranged from about 0.05 up to 0.50 g. Their location is depicted in Fig. 1. Nonetheless, due to lack of acceleration records in the meizoseismal area, these strong-motion time-histories were used in our simulations. At stations where local soil conditions or adjacent structures could have altered the bedrock input motion, numerical 1D or 2D deconvolution analyses were performed (Ref. [2]) to recover the corresponding motion at rock-outcropping.

It should be noted, however, that these motions were recorded within a narrow region located 10 km away from the end of the ruptured zone, in a direction *perpendicular* to it. By contrast, the Kifissos river canyon lies in front of the rupture zone. There is, therefore, strong indication that *forward rupture directivity* could have affected the ground motion in the town of Adàmes. Accounting for near fault effects implies selection time histories that are characterized by a relatively simple long-period pulse of strong-motion and have a relatively short duration. For this purpose, two

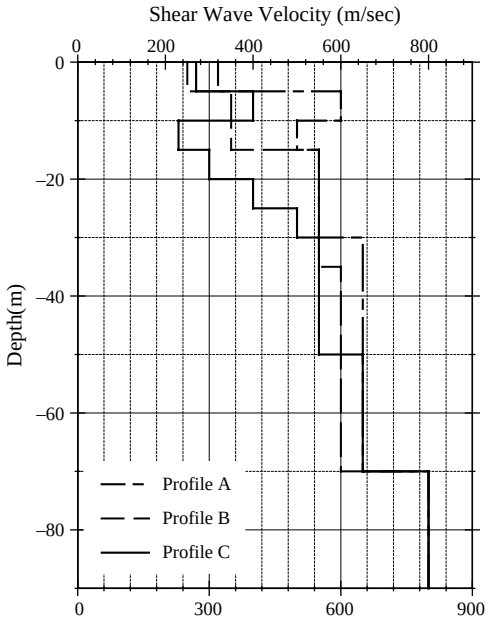


Fig. 3. Shear wave velocity variation with depth for the three characteristic soil profiles in Adàmes (Refs. [3–5]).

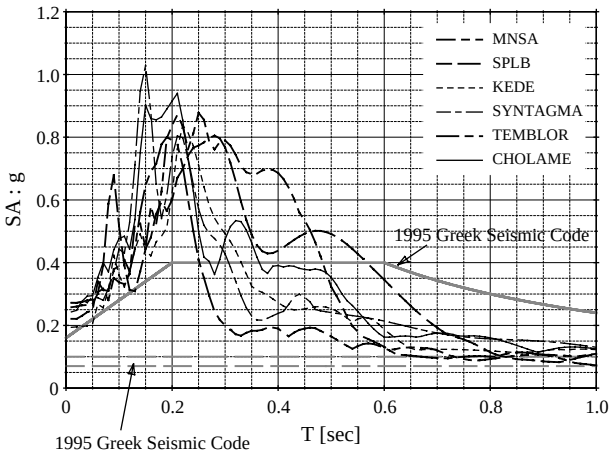


Fig. 4. Acceleration response spectra of strong-motion recordings, defined at rock-outcropping in our simulations(Ref. [4]). Design spectra for the local seismic zone (II), based on the old (1959) and new (1995) Greek Seismic Code Provisions are also shown on the same figure.

historic time-histories were identified in the world strong-motion database (Ref. [2]), obtained during the 1966 $M_s$ 5.6 Parkfield, CA Earthquake at the Cholame Shandon No. 8 and Temblor stations; these records encompass such long-period characteristics.

The response spectra of these six acceleration time-histories, which represent the general strong-motion characteristics of the Athens event and possible directivity effects anticipated at the area of interest, are plotted in Fig. 4. Also shown on the same figure, are the design spectra. For further details on the seismo-tectonics of the event, the geotechnical investigation in Adàmes and the strong-motion data-processing, the reader is referred to Refs. [1–4].

## 3. Elastic simulations

We here investigate the diffraction potential of the slope geometry, the frequency-dependence of topographic amplification and the role of soil layering and material heterogeneity by means of elastic finite-element parametric simulations. The numerical model consists of 25,000 plane 4-node quadrilateral and 3-node triangular finite elements, the size of which was selected on the basis of the frequency content of strong-motion records and the dynamic soil properties, to ensure detailed representation of the propagating wavelengths. Absorbing elements are placed around the discretized domain to avoid spurious reflections into the soil island, and the input motion is prescribed in the form of effective forcing functions at the boundary nodes, to allow for scattered waves impinging onto the boundaries to be absorbed. Successively, the local site conditions are modeled and our results are validated by comparison with aftershock recordings.

### 3.1. Geometry of the topographic feature

Fig. 5 illustrates the wavefield generated by a cliff with the geometry of the Kifissos canyon, at the surface of a homogeneous halfspace upon the incidence of vertically propagating SV-waves. We here use a narrow-band input, namely Ricker wavelet with dimensionless frequency $a_0 = 2f_0h/V_s = 1$, where $f_0$ is the 'characteristic' (central) frequency of the pulse, $h$ is the height of the cliff and $V_s$ is the shear wave velocity of the halfspace. Note that for the slope inclination of the particular topographic feature, the dominant wavelength for the illustrated incident motion ($\lambda_0$) is equal to the lateral dimension of the topographic feature. The Poisson's ratio of the elastic medium is $\nu = 0.35$, typical of stiff clayey soils.

The direct and/or diffracted wavefield shown in Fig. 5 comprises the following waveforms: (i) direct SV waves (denoted SV), (ii) forward scattered Rayleigh waves (denoted R1) generated at the boundaries of the shadow/illuminated zone at the lower corner of the cliff, propagating along the cliff and being forced to change direction at the upper corner, (iii) backward scattered Rayleigh waves (denoted R2) generated at the boundaries of the shadow/illuminated zone at the lower corner of the cliff and propagating outwards; and (iv) surface waves (denoted SP) that are generated along the cliff and propagate upwards approximately with the P-wave velocity. As a result of this, they arrive in the vicinity of the crest almost simultaneously with the direct SV-wave.

The significant enhancement of forward scattered Rayleigh waves (resembling forward directivity effects) by surface waves that are generated along the slope and travel towards the crest with the P-wave velocity, is attributed to the combination of slope inclination and material Poisson's ratio in the illustrated case: for $\nu = 0.35$, critical incidence is calculated as:

$$\theta_{cr} = \arcsin(V_s/V_p) = 28.71^\circ \approx i = 30^\circ$$

Therefore, vertically propagating waves strike at the free surface of the slope with almost critical incidence, and as a result, practically all the incident energy is transformed into surface waves that travel along the slope and *constructively interfere* with the direct SV waves that arrive behind the crest. Therefore, the site conditions in Adàmes satisfy a priori conditions which favor a complicated and *detrimental diffraction potential*, simply by considering the elastic response of the ravine.

Note also that despite the horizontally polarized particle motion of the incident seismic input (vertically propagating SV waves), the surface response contains a parasitic vertical acceleration component as well. This corresponds to the vertical particle motion of surface diffracted waves, and is shown to carry significant portion of the seismic wave energy. For the illustrated case, the amplitude of this

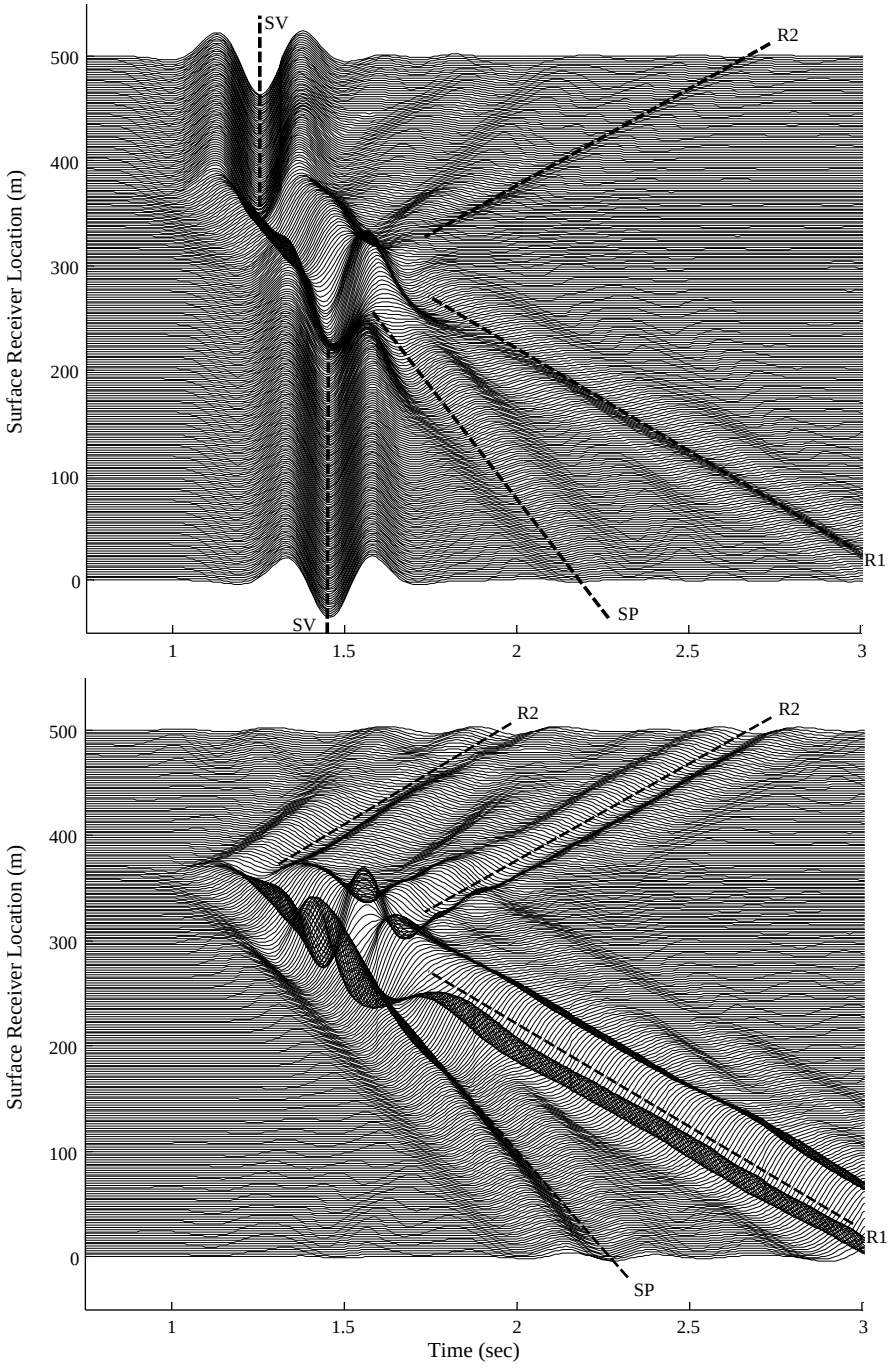


Fig. 5. Synthetics of horizontal (top) and vertical (bottom) acceleration surface response, for a cliff with 30° slope subjected to vertically propagating SV Ricker waves with dimensionless frequency $a_0 = 1.0$

component is on the order of 35% of the peak surface acceleration in the far-field.

### 3.2. Frequency content of incident motion

Fig. 6 illustrates the spatial distribution of peak surface acceleration (horizontal and vertical) behind the crest, for vertically incident SV Ricker wavelets with different central frequencies. The response is normalized by the peak acceleration at the far-field, defined here at distance 300 m from the vertex, where 2D phenomena are shown to be negligible. The main conclusions drawn from our investigation are the following:

(i) Diffraction of seismic waves by topographic irregularities is strongly frequency-dependent. The location of peak horizontal acceleration behind the cliff is controlled by the dominant wavelength ($\lambda_0$) of the incident motion (here the central frequency of

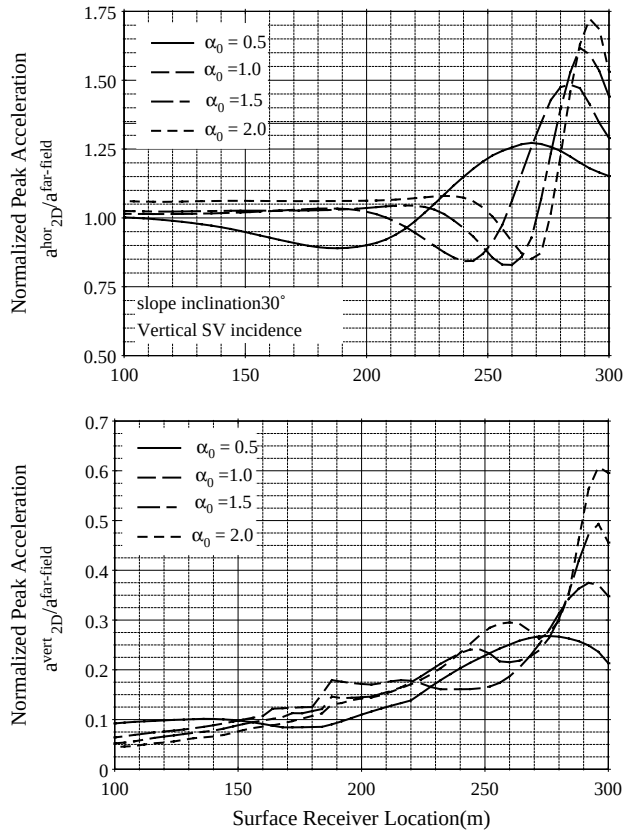


Fig. 6. Normalized horizontal (top) and vertical (bottom) peak surface acceleration behind the crest (located at $x=300$ m), as a function of the frequency content of the incident pulse.

the Ricker wavelet) and is systematically observed at a distance $x=0.2\lambda_0$ from the crest (see also Ref. [6]). The amplitude of peak acceleration at this location is also frequency-dependent, and increases almost linearly with frequency.

(ii) The amplitude of the parasitic acceleration component is also frequency-dependent. For the high-frequency input pulse in these simulations, the peak vertical response is on the order of 60% of the corresponding far-field response. Since the location of peak vertical acceleration is also frequency-controlled, higher frequency components are amplified within a narrower zone in the vicinity of the crest.

(iii) The lobes of constructive and destructive interference at the surface -controlled by the frequency content of the incident waves- result in significant differential motion behind the crest and along the slope, where transition occurs between the convex and concave part of the topography.

We also performed numerical simulations for the case of a homogeneous layer overlying elastic halfspace with various impedance contrasts. Our results show that the bedrock-soil impedance ratio that controls the seismic energy *trapped* in the surface layer and the corresponding one-dimensional amplification of the motion, introduces additional complexity to the problem studied. Resonance of the shallow (in front of the toe) or deep (behind the crest) far-field soil columns not only controls the overall response of the configuration, but indeed enhances the topographic amplification of motion by altering the diffraction mechanism.

The frequency-dependence of the amplification mechanism can be summarized as follows: (i) for a constant input motion, topographic aggravation of the response increases with increasing height of the topographic feature ($h$), and (ii) for a given feature, topographic amplification increases with frequency, yet occurs within a more confined zone in the vicinity of the vertex (it is shown that $\max(a^{hor})$ occurs at $x=0.2\lambda_0$ and $\max(a^{vert})$ at $x=0$ m from the crest)

### 3.3. Soil stratigraphy

We here examine the effects of soil layering by means of a single surface layer with thickness $h_1/h=0.25$ and variable shear wave velocity ($V_{s1}$), overlaying homogeneous halfspace. Results are shown for a soft-surface layer with $V_{s1}/V_s=0.5$, where $V_s$ is the shear wave velocity of the halfspace. This is indeed an idealized model for typical soil profiles in Adàmes, but also for many sedimentary soil deposits.

Fig. 7 illustrates the effects of a surface soft layer on the normalized surface response, by comparison with the homogeneous halfspace ground motion. For further details on the altering of the acceleration wavefield due to the presence of a surface soil layer, the reader is referred to Ref. [5]. From the ensemble of our parametric simulations, the following have been concluded:

(i) The incident wave energy is trapped within the surface layer, and multiple reflections interact with the surface waves that originate from the lower corner of the slope and propagate uphill. The scattered wavefield at the surface comprises Rayleigh waves that are generated at the crest and travel with the Rayleigh wave velocity of the surface layer, $V_{R1}$, and reflections of waves that travel along the layer-halfspace interface with the Rayleigh wave velocity of the later, $V_R$.

(ii) For high-frequency incident waves, the peak normalized horizontal acceleration of the stratified medium is lower than the corresponding of the homogeneous halfspace. Note however that the *absolute* motion amplification is very significant in the soft surface layer case, a fact that illustrates the dominant role of the far-field stratigraphy on the amplification mechanism behind the crest (see Fig. 7(a)).

(iii) The vertical acceleration component is remarkably enhanced. This effect is prominent for incident

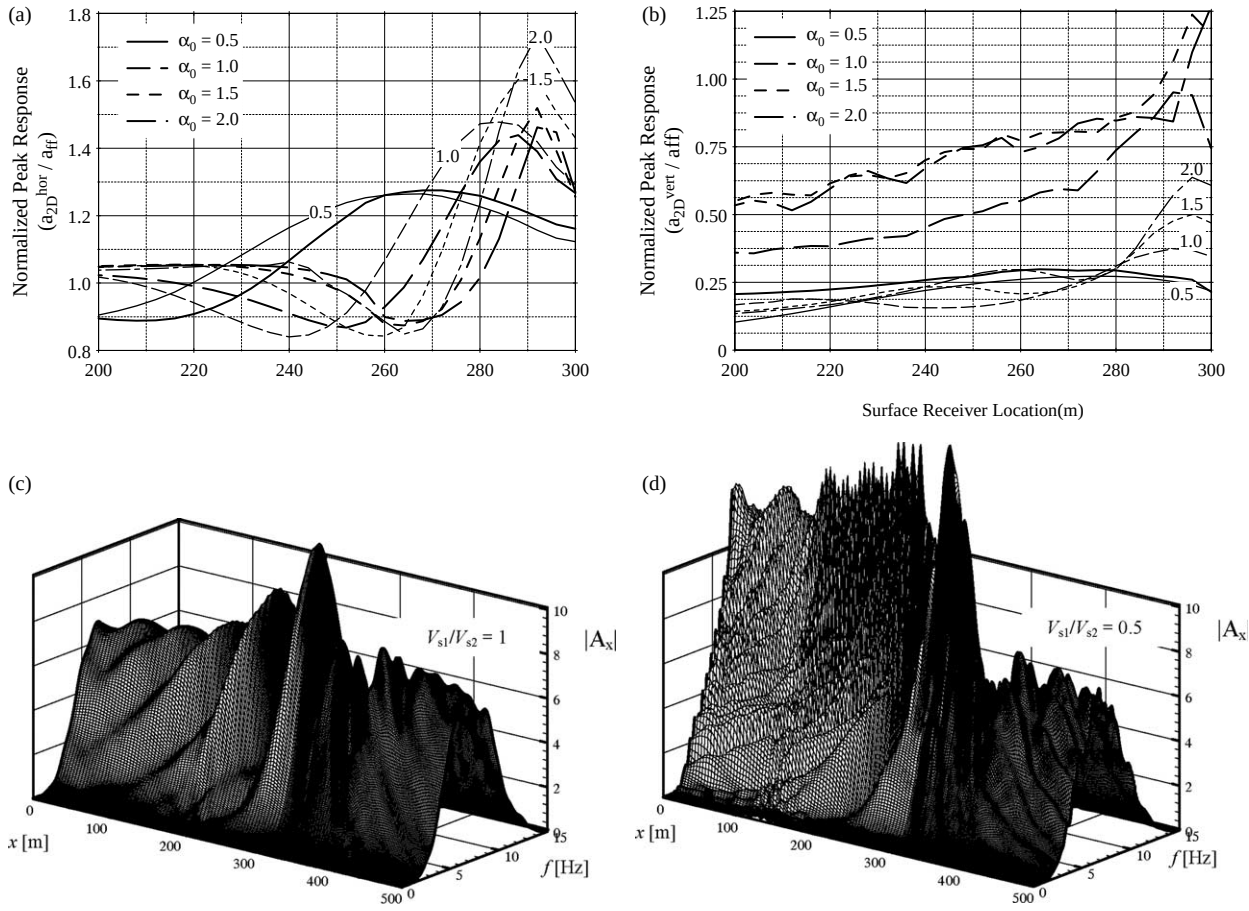


Fig. 7. Normalized peak surface acceleration behind the crest, for a soft surface layer with $V_{s1}/V_s = 0.5$, as a function of the dimensionless frequency $\alpha_0$. (b) Effect of surface layer stiffness ($V_{s1}/V_{s2}$) on the Fourier amplitude surface of surface horizontal acceleration, for a configuration with $h_1/(H-h) = 0.25$, $V_R/V_{s2} = 1$ and $h/H = 0.5$.

waves with wavelengths short enough to see the surface layer. In this case, the vertical acceleration is shown to attain amplitudes 25% larger than the corresponding response at the far-field (see Fig. 7(a)).

(iv) In the frequency domain, the far-field/2D transfer function is very erratic for wavelengths comparable with the thickness of the surface layer, i.e. its resonant frequencies (see Fig. 7(b)).

### 3.4. Lateral heterogeneity

We next investigate the effects of lateral soil heterogeneity on the topographic amplification of seismic motion. For this purpose, we generate Gaussian shear wave velocity stochastic fields using a univariate spectral density function, namely the *exponential decaying* SDF.

$$\rho_i(\xi) = \cos\left[2\tan^{-1}\left(\frac{\xi}{\theta_i}\right)\right] / \left[1 + \left(\frac{\xi}{\theta_i}\right)^2\right]$$

where $\rho_i$ is the correlation function in spatial direction $i$ (horizontal or vertical), $\xi_i$ is the separation distance and $\theta_i$ the correlation distance in the $i$th direction. To account for the mechanism of sediment deposition, we assigned separate correlation structures to the horizontal and vertical direction, and defined the correlation structure of the stochastic field as their product. We then evaluated the effects of correlation distance of the simulated random media, expressed as a function of the dominant wavelengths, by means of Monte Carlo simulations (Ref. [7]). For this purpose, the denormalized random fields were mapped on deterministic finite-element models.

By comparison of the time and frequency-domain characteristics of the response with the homogeneous halfspace case of the same background stiffness, we illustrate phenomenological scattering attenuation for long wavelengths and enhancement of frequency components whose wavelengths are comparable with the horizontal correlation distance of the random medium.

In particular, the spatial distribution of peak normalized surface acceleration is practically the same -or slightly lower- than the halfspace response, yet individual simulations show significant amplification of the vertical component and enhancement of the high-frequencies of the incident motion. In addition, multiple wave reflections at

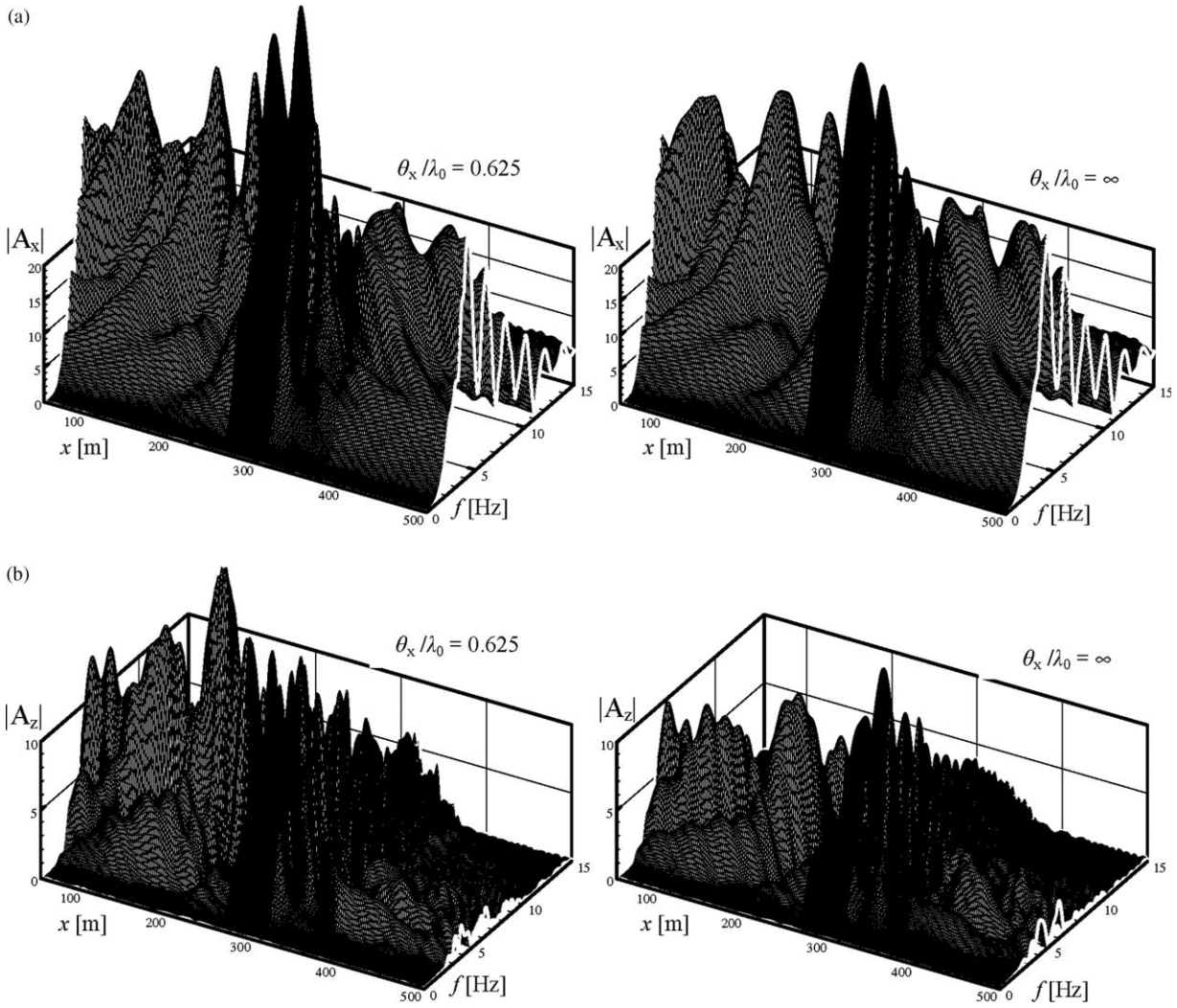


Fig. 8. Fourier amplitude surface of (a) horizontal and (b) vertical response, for random field with $\theta_z/\lambda_0=0.0625$ and $\theta_x/\lambda_0=0.625$ (top) and homogeneous halfspace with the same background velocity ($\alpha_0=2$).

the localized material heterogeneities significantly increase the duration of the surface response (see also Ref. [10]). Fig. 8 illustrates the Fourier amplitude surface of the response behind the crest, for a typical realization of the stochastic field with $\theta_z/\lambda_0=0.0625$ and $\theta_x/\lambda_0=0.625$. Clearly, the erratic frequency content of the response and the amplification level of high frequency components cannot be simulated by means of a homogeneous medium.

### 3.5. Local site conditions and recorded field evidence

The 2D response of the stratified soil configurations corresponding to profiles A, B and C is next evaluated by means of elastic simulations. The numerical model is now subjected to the strong-motion time-histories described above, and results of our analyses can be summarized as follows:

(i) For the broad-band seismic input, topographic amplification occurs within a zone behind the crest, approximately equal to the width of the topographic irregularity ($L=70$ m). This is found to be in accordance with results of our parametric investigation.

(ii) Two-dimensional amplification of the horizontal response is shown to be not very sensitive to soil stratigraphy, yet enhanced in comparison to the homogeneous halfspace case. Peak amplification is of the order of 1.30 $a_{\mathrm{ff}}$, where $a_{\mathrm{ff}}$ is the far-field peak surface acceleration. This is again consistent with amplification computed for $a_0 \approx 4h/\bar{V}_s$ in our parametric study ($\bar{V}_s$ is the mean shear wave velocity of the cliff profile).

(iii) The magnitude of parasitic acceleration however, shows strong dependence on the soil stratigraphy. This effect is primarily controlled by stiffness of the surface layer. In particular, results show that the amplitude of the vertical acceleration range from 0.25 $a_{\mathrm{ff}}$ for the stiffer profile A to 0.70 $a_{\mathrm{ff}}$ for the softer profile C,

where $a_{ff}$ is the corresponding far-field horizontal peak surface acceleration.

Significant corroboration of our elastic numerical simulations comes from two sets of ground motions, recorded during two aftershocks of the Athens 1999 event. The instruments were installed in the free field, two at a site $x \approx 300$ m from the crest, and one at $x \approx 10$ m from the crest (Ref. [3]). The two major aftershocks have provided the *empirical* transfer function spectra that are plotted in Fig. 9. Since the seismographs were placed at locations with different soil property characteristics (profile B for the first two and C for the later), the Fourier spectra evaluated from the aftershock accelerograms have been initially divided by the one-dimensional transfer function for each profile. For the recorded peak accelerations being of the order of 0.015 g, the low-strain dynamic soil properties were used for this purpose. Thus, the variability arising from soil-column flexibility effects has been eliminated.

For the class-A prediction shown in Fig. 9, the stratigraphy of profile C has been used as the background medium stiffness of a Gaussian stochastic field with $\theta_z = 2.5$ m and $\theta_x = 15.0$ m, extrapolated from the geostatistical data of an adjacent site. For the denormalization of the field, a constant standard deviation $\sigma = 0.15\ \bar{V}_s$ has been adopted. The mean and standard deviation of the numerically predicted transfer functions from 20 realizations of the stochastic field at $x = 10$ m are shown in Fig. 9. For the simulations, a Ricker wavelet with central frequency $f_0 = 5$ Hz has been used.

It can readily be seen that the recorded and computed results are in very good agreement, offering strong support to our conclusions. Nevertheless, what should be highlighted herein is that the incorporation of spatial small-strain stiffness variability, and correct calibration of Rayleigh damping coefficients, has proven to be of great importance for the representation of site conditions and subsequent successful prediction of topographic amplification.

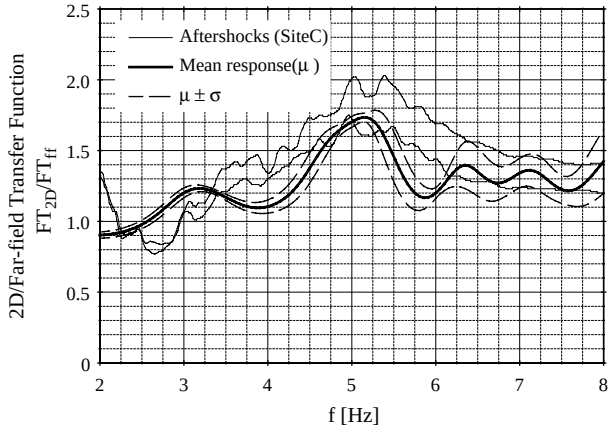


Fig. 9. 2D/Far-field empirical transfer function from the records of two strong aftershocks, and comparison with numerical results of 20 Gaussian stochastic field realizations.

## 4. Non-linear site-specific simulations

### 4.1. One-dimensional site response analysis

The effect of local soil conditions in modifying the intensity and frequency characteristics of ground shaking in Adàmes is first investigated by means of 1D inelastic wave propagation analyses. The far-field profiles A, B, and C are subjected to the six strong-motion time-histories and the surface response is computed in the frequency-domain using an iterative equivalent linear algorithm, and in the time-domain, by incremental non-linear finite-element simulations. For the former, a modified solution was adopted in which the strain-compatible soil properties are frequency-dependent, thus avoiding artificial damping of the high-frequency low-amplitude components of motion (Ref. [8]). For the latter, we used the multi-yield plasticity soil model implemented in the computer code DYNAFLOW (Ref. [9]). For consistency, the parameters controlling the shear behavior of the constitutive model were calibrated to yield the modulus degradation curves (Ref. [10]) used in the equivalent linear solution. The surface response computed by means of the two approaches, is found to be in remarkable agreement. From the ensemble of the analyses performed, the following conclusions are drawn:

(i) Profile A being the stiffest of the three sites, shows an appreciable degree of amplification in the period range of $T < 0.3$ s, where both PGA as well as spectral acceleration (SA) values increase by an average of about 25% compared to the rock-outcrop input motion. However, soil amplification does not alone suffice to explain the observations. Topography and local soil conditions have equally contributed to the observed damage distribution at this site, which was more intense next to the crest. In fact, for this stiff and relatively homogeneous profile, the moderate damage intensity can be even justified by means of our elastic 1D and 2D analyses (recall $a_{2D}/a_{ff} = 1.3$ for profile A).

(ii) Profile B is softer than profile A, and simulations show larger amplification over a wider period range. Computed PGA values are in the range of 0.30–0.40 g, and the highest SA reaches 1.50 g at $T \approx 0.2$ s. Evidently, there is a pseudo-resonance condition occurring at this period: the fundamental period of the soil column ($T_{soil} \approx 0.2$ s from the surface/rock-outcrop transfer function) nearly coincides with the dominant excitation period ($T_{input} \approx 0.2$ s). The dominant role of soil conditions becomes evident for this site, where the damage intensity was similar next to the crest and in the far-field.

(iii) Profile C is the softest of the three sites. The fundamental natural period of the soil deposit at the last step of the iteration process is estimated $T_{soil} \approx 0.72$ s, whilst most of the rock-outcrop

excitations have much smaller dominant periods, $T_{input} \approx 0.1$–$0.2$ s. Hence, no increase or even deamplification is expected in PGA and in SA values due to local soil conditions for $T < 0.25$ s, a fact confirmed with our results. On the other hand, the spectral amplification predicted for periods 0.4–0.6 s, could be substantial if the input motion were rich in such relatively long-period components. In summary, moderate elastic topographic amplification of 30% and simultaneous 1D inelastic soil deamplification do not reconcile with the observations for this profile, characteristic of one of the most heavily damaged regions in the 7-9-99 earthquake.

### 4.2. Two-dimensional analyses

We next perform 2D inelastic simulations and investigate the effects of material softening on the 2D amplification of surface motion. To simulate the inelastic soil response, we perform: (i) 2D elastic analyses with strain-compatible soil properties computed at the last iteration of the 1D iterative solution, and (ii) time-domain 2D non-linear analyses using the multi-yield surface plasticity model. The surface response is again normalized by the far-field motion, which was found to be consistent for the two methods. A more useful measure of topographic amplification in the frequency domain is the response spectral ratio of the 2D horizontal acceleration component to the corresponding far-field response. In the ensuing, we shall refer to this ratio as Topographic Aggravation Factor (TAF). The mean TAF at $x = 20$ m from the crest is plotted in Fig. 10 as a function of period ($T$), for profile C and the ensemble of strong input motions.

As can readily be seen, the elastic and equivalent linear solution yields very similar spectral amplification values, whereas the inelastic solution shows significant enhancement of the high frequency components. This can be justified when we consider that the incremental variation of strain-compatible soil properties introduces a posteriori randomness in the original horizontally stratified profile that has been shown to favor amplification of short wavelength components. It is indeed in the high-frequency regime that theoretical elastic models fail to predict measured amplification levels in the field. Note also that the elastic finite-element solution is shown to be sensitive in the correct selection of Rayleigh damping coefficients, which when calibrated for the mean frequency of the input motion, artificially attenuate the high-frequency components.

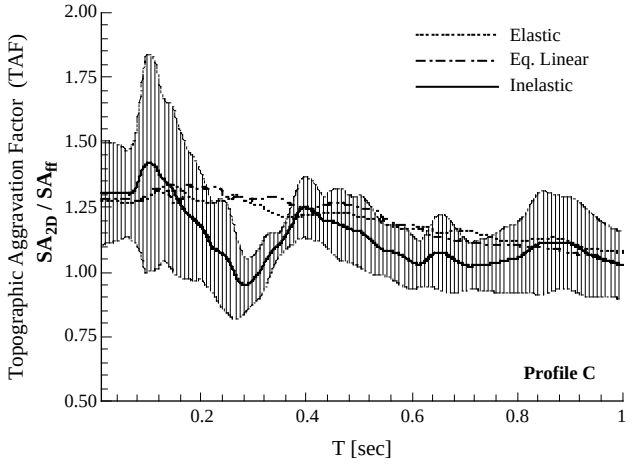


Fig. 10. Mean spectrum of topographic aggravation factor at $x = 20$ m from the crest, for profile C and six strong-motions.

For larger periods ($T > 0.2$ s), the spectrum of TAF shows that in the period range $0.2\text{ s} < T < 0.4$ s, where no 1D amplification occurs for the particular profile, topography effects are negligible. They become important again in the period range $0.4\text{ s} < T < 0.6$ s, which coincides approximately with the so-called *topographic* frequency (see Ref. [7]), determined from the location where maximum amplification of motion behind the crest occurs (recall that this is $h/\lambda_0 = 0.2$ for a homogeneous soil profile). For the stratified soil configuration, this can be approximated by $5h/\bar{V}_s$.

Amplification of high-frequencies is more pronounced when material heterogeneity (a priori randomness) is also introduced in the simulations. A more realistic random small-strain stiffness field is here simulated as a non-Gaussian stochastic field, where the theoretical correlation structures have been fitted to available geostatistical data from an adjacent site (Ref. [11]). The spatial distribution of peak surface response is shown in Fig. 11 for profile C. The spectrum of TAF at $x = 20$ m from the crest is compared to that obtained from the inelastic wave propagation analysis of the horizontally stratified configuration in Fig. 11.

The erratic surface response, which is substantially amplified and more confined in the vicinity of the crest, is consistent with the enhancement of high-frequencies, when material heterogeneity and inelastic soil behavior are modeled. Ref. [11] illustrates that for 1D conditions, strong-motion input introduces material yielding that is prominent in the horizontal direction and overshadows the small fluctuations of the stochastic small-strain field; this effect yields the horizontally stratified configuration adequate for seismic response analyses of weakly heterogeneous formations. This is no longer valid for 2D wave propagation analyses, where the localization of material yielding is controlled by diffracted rather than direct waves, and does not restore the background medium stratigraphy when non-linear effects occur.

Even more important for the justification of the damage distribution in site C is the amplitude of the vertical acceleration component, which attains values $0.8a_{ff} - 1.0a_{ff}$ near the crest. This is consistent with the results of our parametric analyses that show amplification of the parasitic response for a soft surface layer.

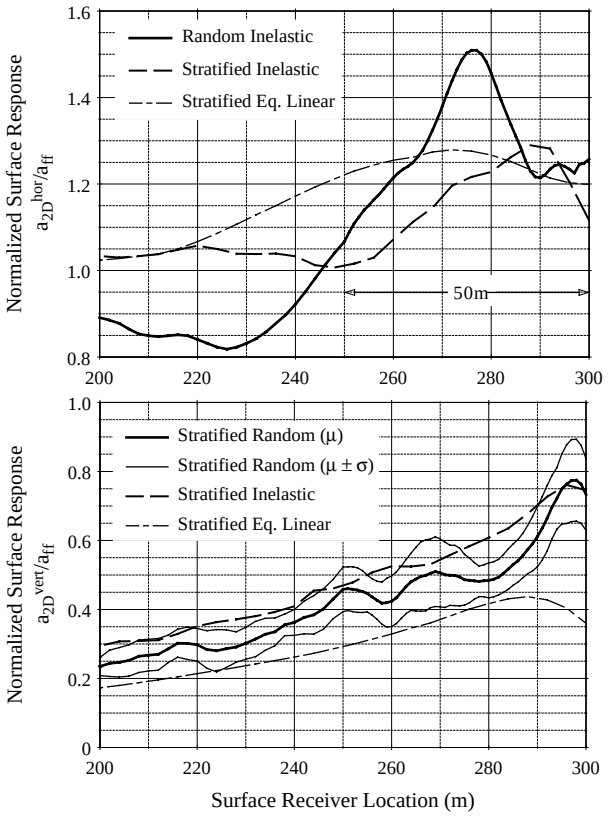


Fig. 11. Mean normalized peak acceleration for profile C and a random medium with the same mean stiffness and $\theta_z=2.5$ m and $\theta_x=16.0$ m, subjected to six strong-motions.

## 5. Soil–structure interaction

We next investigate the effects of soil–structure interaction on the diffraction mechanism of seismic waves by cliff-type topographies, for a structure founded in the vicinity of the vertex. The structure is modeled as a solid block with density $\rho_{str}=0.4$ mg/m$^3$, accounting for the macroscopic properties of the structural system, and Poisson's ratio $\nu=0.20$; its height is 16.0 m for all simulations, corresponding to a 4-story building with 4.0 m mean story-to-story spacing. A schematic representation of the numerical model is shown in Fig. 12. It should be noted that in our simulations, no relative displacement is allowed at the soil–structure interface.

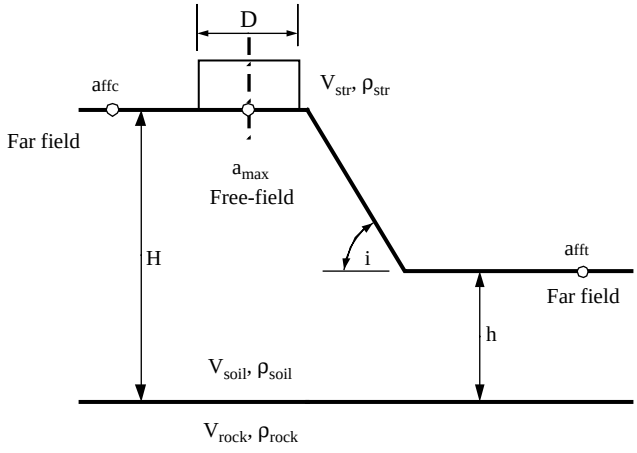


Fig. 12. Schematic illustration of the numerical model used for simulations of elastic soil–structure interaction in the vicinity of the crest.

### 5.1. Elastic parametric simulations

We first conduct elastic parametric analyses, where the underlying soil is simulated as a homogeneous halfspace with density $\rho_{soil}=2.0$ Mg/m$^3$ and Poisson's ratio $\nu=0.35$. The centerline of the simulated structure is located at a distance $x/\lambda_0=0.2$ from the crest ($\lambda_0$ is the dominant propagating wavelength of Ricker wavelets), where peak topographic aggravation was determined for the response of a homogeneous halfspace. The dimensionless parameters that govern the response of this system are: (i) the horizontal dimension of the structure, normalized by the dominant propagating wavelength ($D/\lambda_0$), and (ii) the structure-soil impedance ratio ($r=(\rho V_s)^{str}/(\rho V_s)^{soil}$), which controls the amount of energy reflected at their interface.

Fig. 13(a) illustrates plan views of the Fourier amplitude surface of horizontal and vertical acceleration along the surface, for the structure-soil impedance ratios $r=0.5$ (relatively soft structure) and $r=5.0$ (relatively stiff structure). In both figures, the response of the *free-field* ($r=0$) is also shown for comparison. Seismogram synthetics of the same configurations, upon incidence of Ricker wavelets with dominant wavelength $L/\lambda_0=1.25$ are shown Fig. 13(b). The main conclusions that can be drawn from our parametric investigation can be summarized as follows:

(i) The effects of soil–structure interaction on the time- and frequency-domain characteristics of the response, are not confined at the location of the structure, but extend both towards the far-field as well as along the cliff. These effects are strongly frequency-dependent; for the particular problem studied, the propagating wavelengths need to be of the same order of magnitude with the horizontal dimension of the structure (or shorter) to *experience* the geometric constrains imposed by the rigidity of the foundation.

(ii) In the time-domain, trapping of the incident and diffracted waves within the structure results in significant enhancement of the vertical acceleration component and deamplification of the horizontal response at the location of the structure, compared to the free-field response. This phenomenon is attributed to the rotational path that the trapped diffracted waves follow within the structure, which imposes intense rocking motion. The intensity of vertical motion decreases with increased structural stiffness; this effect results from the inability of the rigid structure to follow the strongly differential motion.

(iii) The seismogram synthetics in Fig. 13(a) illustrate that for relatively soft structures and short wavelengths, the structural response results in continuous wave emission towards the slope, evident both for the horizontal and vertical components. For rigid structures, the backward reflection of surface waves appears as a single enhanced wave that travels towards the base of the cliff.

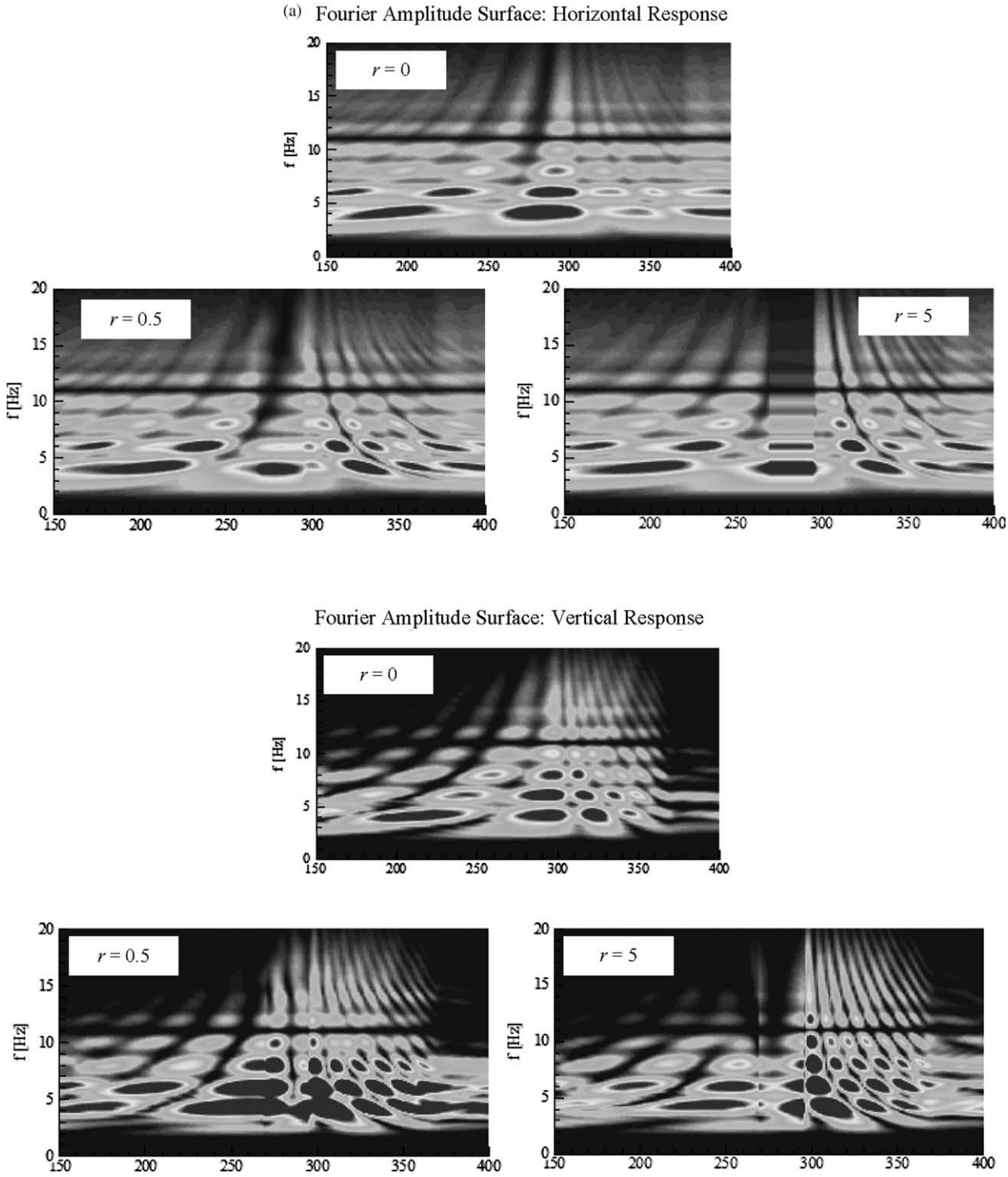


Fig. 13. a Plan view of Fourier amplitude surface of ground surface response (horizontal component in top and vertical component in bottom figure) of the configuration, subjected to a sequence of vertically propagating SV-Ricker wavelets with $D/\lambda_0 = 0.375$, 0.625 and 1.25, for structure-soil impedance ratios $r =$ 0.5 and 5. The homogeneous layer case ($r = 0$) is also plotted for comparison. b. Seismogram synthetics of ground surface acceleration (horizontal component in top and vertical component in bottom figure), subjected to vertically propagating SV-Ricker waves with $D/\lambda_0 = 1.25$, for structure-soil impedance ratios $r =$ 0.5 and 5.0.

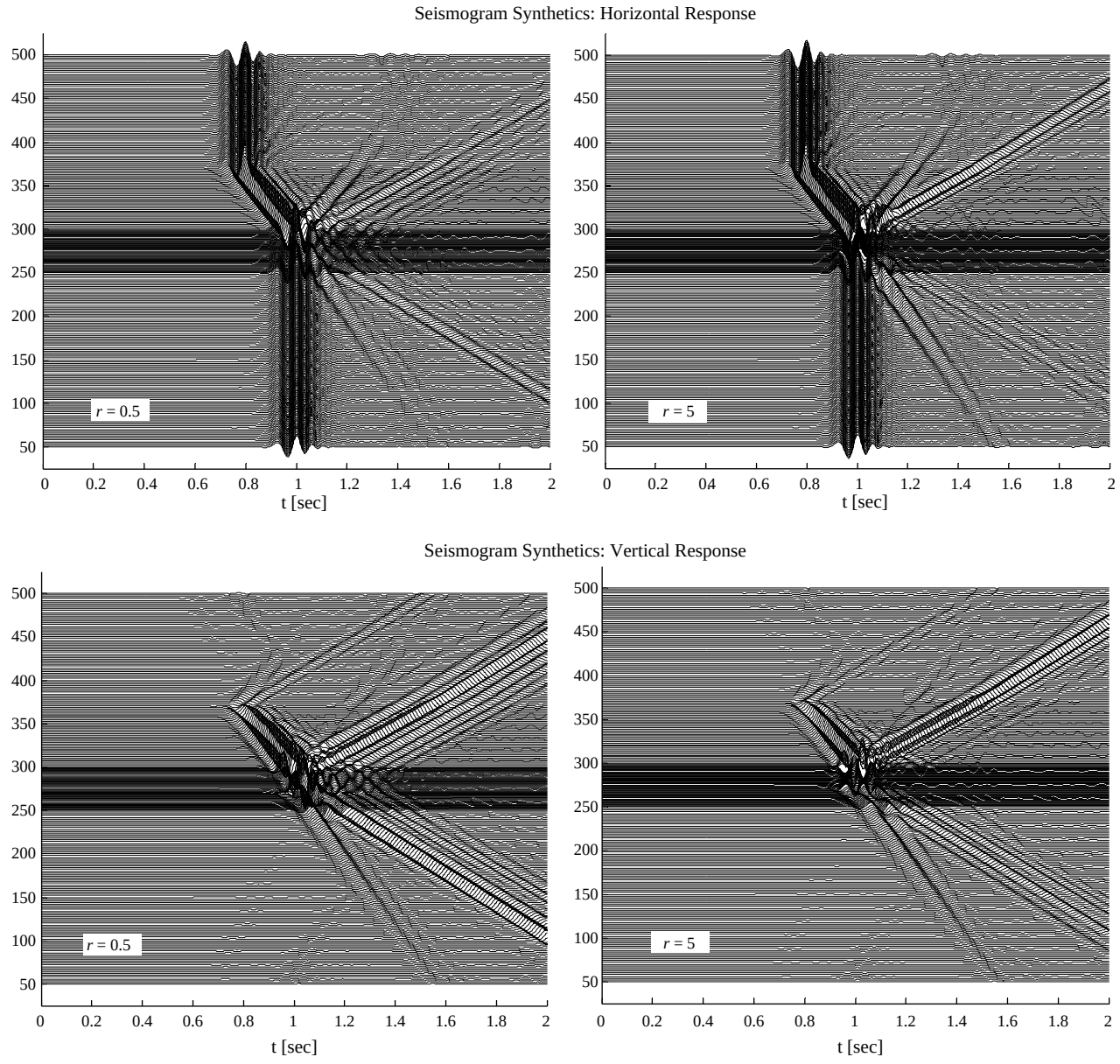


Fig. 13 (*continued*)

(iv) Finally, frequency domain results clearly reveal both the geometric inability of the structure to follow the erratic soil response behind the crest, and the enhancement of the vertical component. This can readily be seen in Fig. 13(b), where high-frequency components of both horizontal and vertical acceleration are completely filtered out at the location of the stiff structure ($r=5.0$), whereas for the soft structure, the rocking motion enhances the vertical response at the location of the structure and along the crest.

### 5.2. Non-linear site-specific simulations

To account for inertial interaction and study the response of a rigid structure founded next to the crest, we conducted non-linear 2D analyses. For relatively soft soil formations, repeated loading on structures creates a zone of yielding and inelastic deformation beneath the foundation. This reduces the effective dynamic impedance (radiation damping) of the semi-infinite domain and creates resonant frequencies at which the structural motion is amplified. This phenomenon is similar to the numerical observation of Borja et al. [12] for a vertically oscillating footing on the surface of an elastoplastic halfspace.

On the other hand, upon incidence of seismic waves, soil deformations impose subsequent dynamic displacements onto the foundation and the supported structure (*kinematic* interaction). In turn, this induced motion of the super-structure, generates inertia forces that result in dynamic

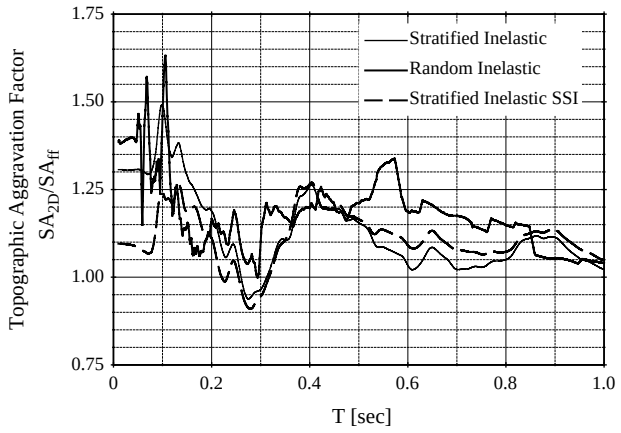


Fig. 14. Schematic illustration of numerical model, and mean spectrum of topographic aggravation factor at $x=20$ m from the crest, for profile C and six strong-motions.

forces and moments at the base, subsequently transmitted into the supporting soil. Therefore, additional deformations are imposed on the surrounding soil while additional waves emanate from the soil-foundation interface (so-called *inertial* interaction).

Our preliminary investigation on soil–structure interaction effects for soil profiles A, B and C in absence of the topographic irregularity, showed that the response of typical local structures (2- to 4-storey concrete buildings) when subjected to quasi-static horizontal, vertical, and seismic loading, do not produce significant inelastic effects; this is attributed to the low weight of the structural system and the relatively high stiffness of the underlying soil formations. Nonetheless, the presence of the structure at the location of peak topographic aggravation alters the wavefield direction and the corresponding strain-induced material softening; this effect is strongly-dependent on the soil–structure impedance ratio.

For the stiff soil formations of Adàmes, altering of the response at the location of the structure is shown to be governed by kinematic interaction phenomena, namely the inability of the structure to follow the strongly differential surface response. In particular:

(i) The coherent response of the structure reduces the erratic spatial distribution of peak horizontal acceleration that characterizes the free-field motion. The level of topographic aggravation close to the vertex is shown to be on the same order of magnitude for the two problems. For the softer profiles B and C in particular, the presence of the structure is shown to have beneficial effects for high-frequency seismic input motions. In these cases, *kinematic* interaction results in reduction of the motion topographic aggravation, when compared to the free-field response at the same location.

(ii) The peak vertical acceleration is shown to be of the same order of magnitude for all cases analyzed. The vertical component is significantly enhanced by the rocking response of the structure, which is associated with the inclined reflected and diffracted waves comprising the structural seismic input.

Time and frequency-domain results are shown for the stratigraphy of profile C in Fig. 14. For the latter in particular, the spectrum of TAF at the centerline of the structure is compared to the free-field response at the same location. Note that the high-frequency components of the response are *geometrically* filtered, yet for higher periods, the frequency content of motion is practically unaffected by the presence of the structure. This verifies that no significant inelastic effects have resulted from the structural static loading or inertial soil–structure interaction.

## 6. Conclusions

Using a case study from the Athens 1999 earthquake, we have shown that: (i) despite the detrimental diffraction potential of the cliff, geometry alone could not predict the high level of experienced damage, (ii) even stiff soil sites (with average $V_s=400$ m/s at the top 30 m) can substantially amplify seismic motions, (iii) soft surface layers significantly aggravate the amplitude of parasitic acceleration, which cannot be neglected for design purposes, (iv) weak motion data can be successfully used as a valuable guidance in reconnaissance studies, but they are not adequate to describe topography effects associated with strong-motions, (v) 2D inelastic soil response introduces localized patches of yielded material, which equivalently to a random medium, amplify high-frequency components and further enhance the vertical response and reduce the radiation damping, (vi) soil–structure interaction on stiff soil deposits filters the high frequencies of the horizontal motion.

## References

[1] Pavlides SB, Papadopoulos G, Ganas A. The fault that caused the Athens September 1999 Ms=5.9 Earthquake: field observations. Nat Hazards 2002;27(1-2):61–84.

[2] Gazetas G, Kallou PV, Psarropoulos PN. Topography and soil effects in the $M_S$ 5.9 Parnitha (Athens) Earthquake: the case of Adámes. Nat Hazards 2002;27(1–2):133–69.

[3] Gazetas G. The 1999 Parnitha (Athens) Earthquake: soil effects on distribution of damage. In: Ansal A, editor. Proceeedings of 15th international conference on soil mechanics and geotechnical engineering: lessons learned from recent strong earthquakes, Istanbul, 2001. p. 5–18.

[4] Gazetas G. Analytical and experimental evaluation of ground accelerations in the meizoseismal region of the Athens 1999 Earthquake. Research report, Organization of Antiseismic Protection (OASP), Athens 2001;1–3.

[5] Assimaki D, Gazetas G. Soil and topographic amplification on canyon banks and the Athens 1999 earthquake. J Earthq Eng 2004;8(1):1–44.
[6] Ashford SA, Sitar N, Lysmer J, Deng N. Topographic effects on the seismic response of steep slopes. Bull Seismol Soc Am 1997;87(3): 701–9.
[7] Popescu R. 'Stochastic variability of soil properties: data analysis, digital simulation, effects on system behavior,' PhD Thesis, Princeton University, Princeton, NJ; 1995.
[8] Kausel E, Assimaki D. Simulation of dynamic, inelastic soil behavior by means of frequency-dependent shear modulus and damping. J Eng Mech, ASCE 2001;128(1):34–47.
[9] Prevost JH. 'DYNAFLOW: a nonlinear transient finite element analysis program.' Technical report, Department of Civil Engineering and Operations Research, Princeton University, Princeton, NJ; 1981.
[10] Vucetic M, Dobry R. Effect of soil plasticity on cyclic response. J Geotech Eng 1991;117(1):89–107.
[11] Assimaki D, Pecker A, Popescu R, Prevost JH. Effects of spatial variability of soil properties on surface ground motion. J Earthq Eng 2003;7(1):1–44.
[12] Borja RI, Wu WH, Smith HA. Nonlinear Response of vertically oscillating rigid foundations. J Geotech Eng 1993; ASCE, 119, 893–911.